Electronic Supporting Information

for

Syntheses and Properties of Phosphine-Substituted Ruthenium(II) Polypyridine Complexes with Nitrogen Oxides

Go Nakamura,[ab] Mio Kondo,[abcd] Meredith Crisalli,[e] Sze Koon Lee,[a] Akane Shibata,[a] Peter C. Ford,[e] and Shigeyuki Masaoka*[abd]

[a] Institute for Molecular Science (IMS), 5-1 Higashiyama, Myodaiji, Okazaki, Aichi 444-8787, Japan.

[b] Department of Structural Molecular Science, School of Physical Sciences, SOKENDAI (The Graduate University for Advanced Studies), Shonan Village, Hayama-cho, Kanagawa 240-0193, Japan.

[c] ACT-C, Japan Science and Technology Agency (JST), 4-1-8 Honcho, Kawaguchi, Saitama, 332-0012.

[d] Research Center of Integrative Molecular Systems (CIMoS), Institute for Molecular Science 38 Nishigo-naka, Myodaiji, Okazaki, Aichi 444-8585, Japan.

[e] Department of Chemistry and Biochemistry, University of California at Santa Barbara, Santa Barbara, California 93106-9510, United States

E-mail: masaoka@ims.ac.jp

Table of Contents

Reaction of the nitrite complexes with acid

Reactions of *nitrito*-κ*N* complexes with hexafluorophosphoric acid (HPF$_6$) were studied. Only **cis-NO$_2$** showed large blue shift of MLCT band from 431 nm to 383 nm, suggesting the formation of a corresponding nitrosyl complex. In contrast, **trans-NO$_2$** and **PP-NO$_2$** reacted with HPF$_6$ and changed to solvent coordinated complexes (Figures S1-2). This may be due to easy dissociation of the N(O)OH ligand at the *trans* position of the phosphino group in **trans-NO$_2$** or **PP-NO$_2$**.
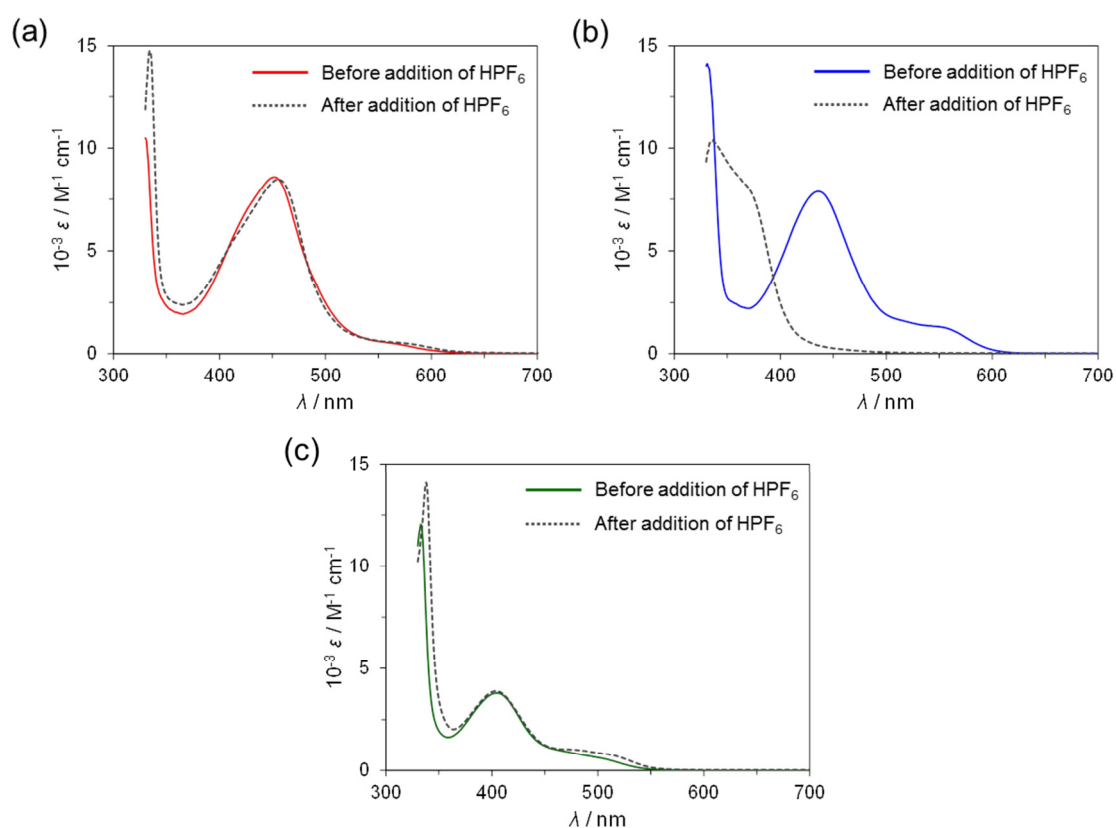

Figure S1 UV-vis absorption spectra of (a) **trans-NO$_2$**, (b) **cis-NO$_2$**, and (c) **PP-NO$_2$** in acetone at 0 °C before and after the addition of a few drops of HPF$_6$.
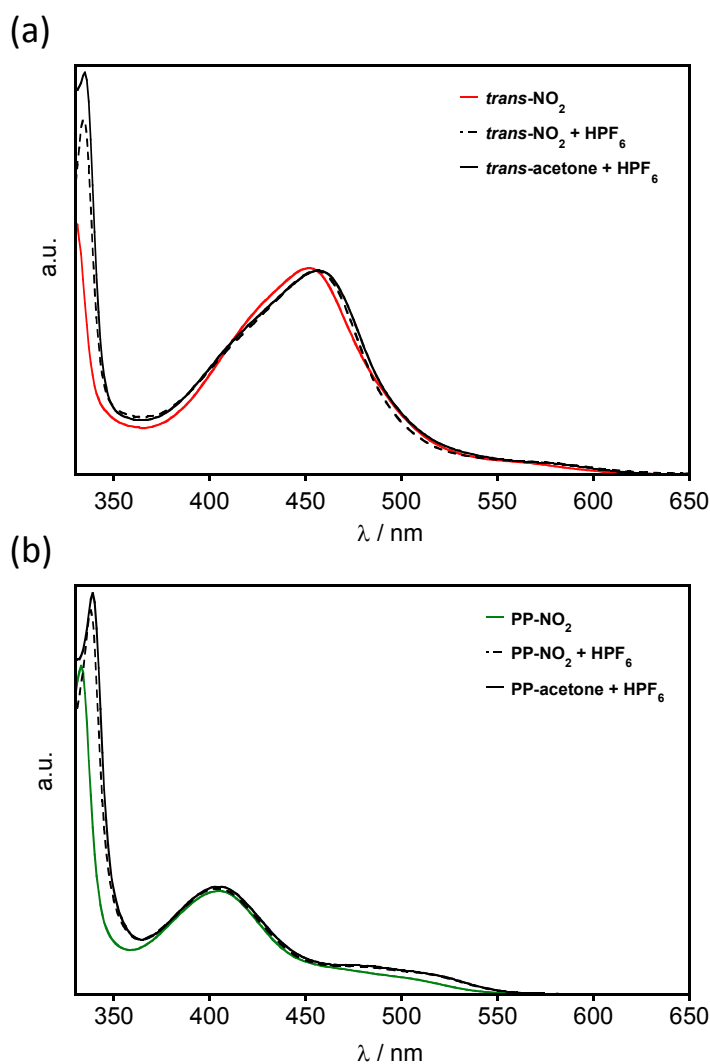
Figure S2 (a) UV-vis absorption spectra of ***trans*-NO$_2$** before (red solid line) and after (black dashed line) the addition of a few drops of HPF$_6$ and ***trans*-acetone** in the presence of a few drops of HPF$_6$ (black solid line) in acetone. (b) UV-vis absorption spectra of **PP-NO$_2$** before (green solid line) and after (black dashed line) the addition of a few drops of HPF$_6$ and **PP-acetone** in the presence of a few drops of HPF$_6$ (black solid line) in acetone. The spectra of *nitrito-*κ*N* complexes after the addition of HPF$_6$ are almost identical to those of corresponding acetone complexes, which indicates the formation of the solvent coordinated complexes.
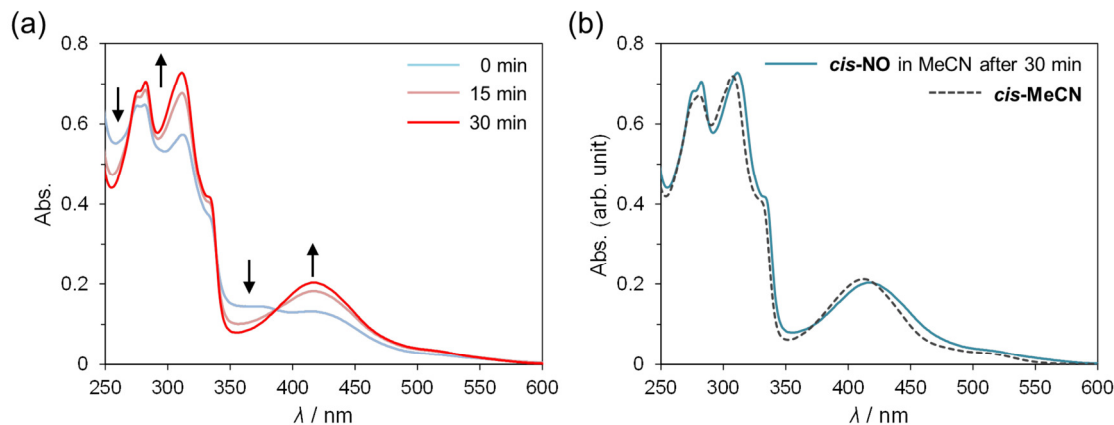
Stability of *cis*-NO in Various Solvents

Figure S3 (a) UV-vis absorption spectral changes of ***cis*-NO** in MeCN at room temperature. ***cis*-NO** is gradually converted to solvent coordinated form, ***cis*-MeCN** in MeCN. (b) A UV-vis absorption spectrum of ***cis*-NO** in MeCN after 30 min and that of ***cis*-MeCN** in MeCN. There are two possible pathways for the decomposition: (1) the dissociation of NO and subsequent reduction of the formed Ru(III) complex, and (2) the dissociation of NO^+ to form the Ru(II) complex. In this study, we could not determine which path is more favourable because the detection of the released NO+ is difficult.

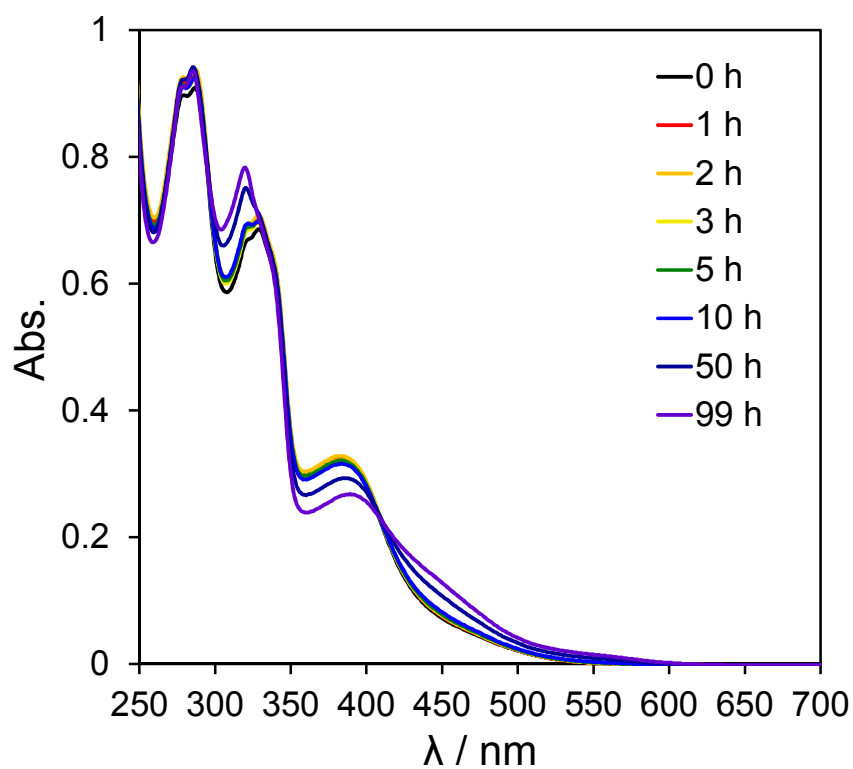**Figure S4** Time course changes of UV-vis absorption spectra of *cis*-**NO** in ethylene glycol at room temperature. *cis*-**NO** exhibited almost no change 3 h after the preparation of the solution, whereas the gradual change was observed after 50 h.

DFT Calculations.

To discuss the electronic structures of **_trans_-NO$_2$**, **_cis_-NO$_2$**, and **PP-NO$_2$**, density functional theory (DFT) calculations were conducted using the Gaussian 09 programs with the B3LYP functional and LanL2DZ basis set. All calculations were performed with the polarizable continuum model (PCM) to account for solvent effects in acetonitrile. All optimized structures were shown in Figure S5.

The highest occupied molecular orbitals (HOMOs, HOMO to HOMO−2) and the lowest unoccupied molecular orbitals (LUMOs, LUMO to LUMO+2) are illustrated in Figure S6. The HOMOs of **_trans_-NO$_2$** and **_cis_-NO$_2$** contain dπ (d_{xy}, d_{yz}, and d_{zx}) characteristics of ruthenium with distribution to the π^* orbitals of trpy, Pqn, and acetonitrile ligands and σ^* orbitals of P−C bonds in the phosphine donors. The LUMOs are dominated mainly by π^* orbitals of trpy or Pqn. The frontier orbitals of **PP-NO$_2$** are similar to those of **_trans_-NO$_2$** and **_cis_-NO$_2$**, except that the π^* orbitals of dppbz are not involved in orbitals from HOMO−2 to LUMO+2. The HOMO energy levels of **_trans_-NO$_2$**, **_cis_-NO$_2$**, and **PP-NO$_2$** were −6.04, −6.06, and −6.31 eV (Figure S7), respectively, indicating a tendency similar to that observed in the oxidation potentials (E_{pc}) in cyclic voltammograms (0.79, 0.82, and 0.95 V vs Fc/Fc$^+$).

Electronic transitions for the complexes were investigated using the time-dependent density functional theory (TD-DFT) method. Calculated excitation wavelengths and oscillator strengths for selected transitions are listed in Table S1, and absorption spectra based on these calculated transitions with Gaussian functions are depicted in Figure S8. The profiles of convoluted absorption spectra are similar to those observed experimentally. For **_trans_-NO$_2$** and **_cis_-NO$_2$**, transitions in the visible light region arise mainly from the MLCT transition from the dπ orbitals of ruthenium (HOMOs) to the π^* orbitals of trpy (LUMO and LUMO+1) and Pqn (LUMO+2). For **PP-NO$_2$**, the transitions arise mainly from dπ orbitals of ruthenium (HOMOs) to π^* orbitals of trpy (LUMO and LUMO+1), which do not involve the π^* orbitals of dppbz. Intensity of the simulated absorption of **PP-NO$_2$** was nearly 50% of those of **_trans_-NO$_2$** and **_cis_-NO$_2$**, which is consistent with the experimental results (Figure 3).
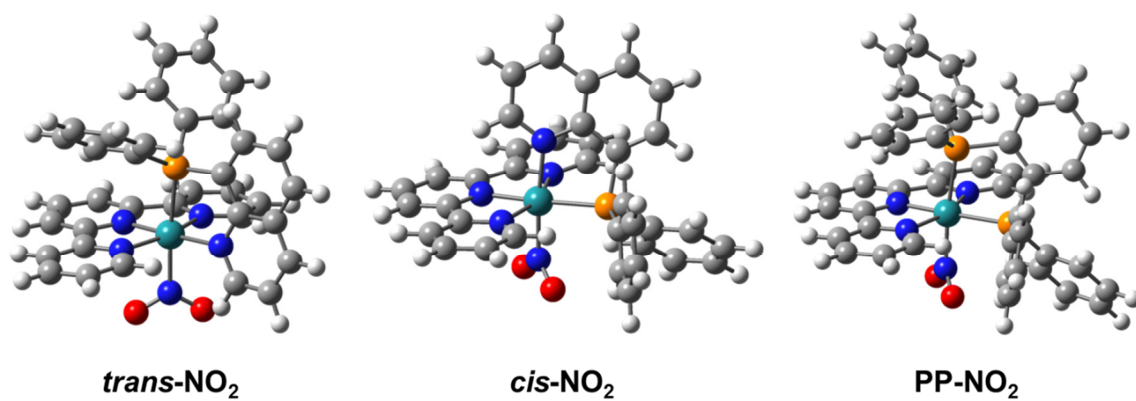
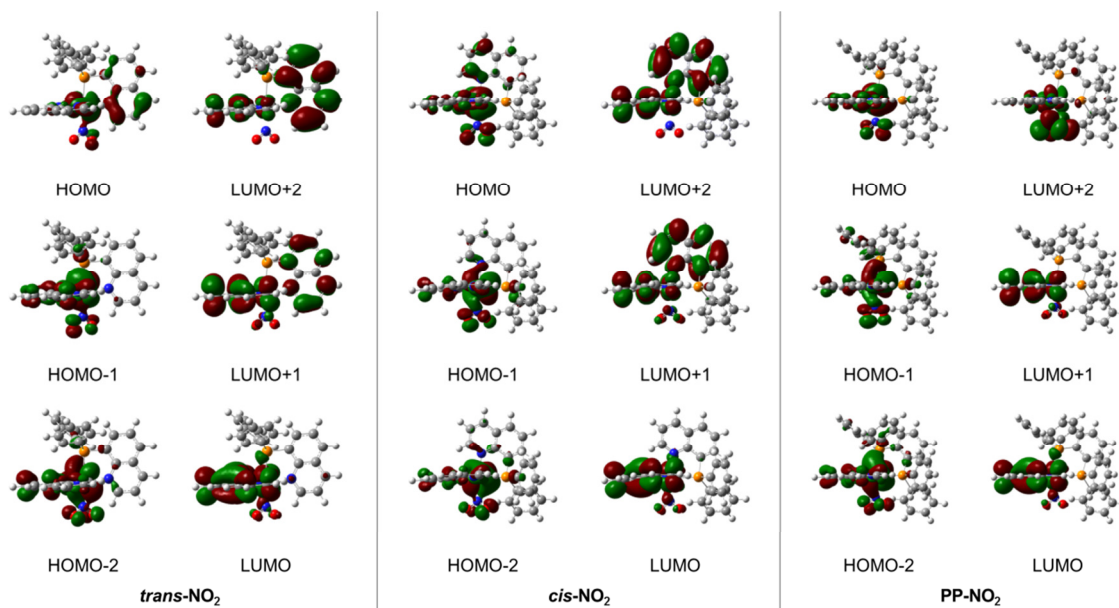**Figure S5** Optimized structures of cationic moieties of ***trans*-NO₂**, ***cis*-NO₂**, and **PP-NO₂**.

Figure S6 Isodensity surface plots of selected frontier molecular orbitals of ***trans*-NO₂**, ***cis*-NO₂**, and **PP-NO₂** based on the optimized ground-state geometry.
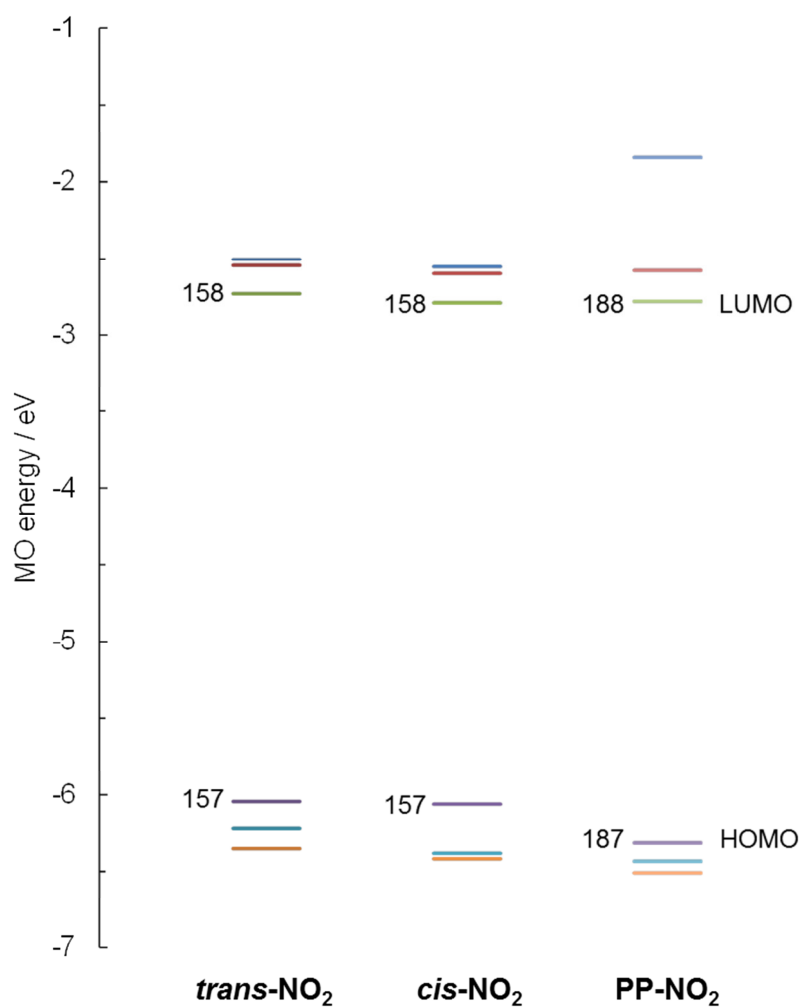
Figure S7 Diagram of DFT-derived molecular orbital energies of *trans*-NO₂, *cis*-NO₂, and **PP-NO₂**.

Table S1 Calculated TD-DFT excitation energies of *trans*-NO$_2$, *cis*-NO$_2$, and **PP-NO$_2$** in acetonitrile media. f denotes the oscillator strength calculated for each transition.

| Complex	λ / nm	f	Transition			|CI coef| (> 0.3)
trans-NO$_2$	440.86	0.0681	HOMO–2	$\rightarrow$	LUMO	0.49267
			HOMO	$\rightarrow$	LUMO+2	0.37097
	434.46	0.0589	HOMO–1	$\rightarrow$	LUMO+1	0.30404
			HOMO	$\rightarrow$	LUMO+2	0.49097
	411.01	0.0260	HOMO–2	$\rightarrow$	LUMO+1	0.40021
			HOMO–1	$\rightarrow$	LUMO+2	0.31482
	404.06	0.0341	HOMO–2	$\rightarrow$	LUMO+1	0.53011
cis-NO$_2$	436.63	0.0714	HOMO	$\rightarrow$	LUMO+2	0.49267
	420.79	0.0489	HOMO–2	$\rightarrow$	LUMO	0.30590
			HOMO–2	$\rightarrow$	LUMO+1	0.34591
			HOMO–1	$\rightarrow$	LUMO	0.32855
			HOMO	$\rightarrow$	LUMO+1	0.33384
	415.44	0.0200	HOMO–1	$\rightarrow$	LUMO+1	0.63146
	407.86	0.0246	HOMO–2	$\rightarrow$	LUMO+1	0.58333
PP-NO$_2$	413.93	0.0299	HOMO–2	$\rightarrow$	LUMO+1	0.32625
			HOMO–1	$\rightarrow$	LUMO+1	0.35894
			HOMO	$\rightarrow$	LUMO+1	0.37271
	402.79	0.0364	HOMO–1	$\rightarrow$	LUMO+1	0.59003
	390.03	0.0317	HOMO–2	$\rightarrow$	LUMO+1	0.60400
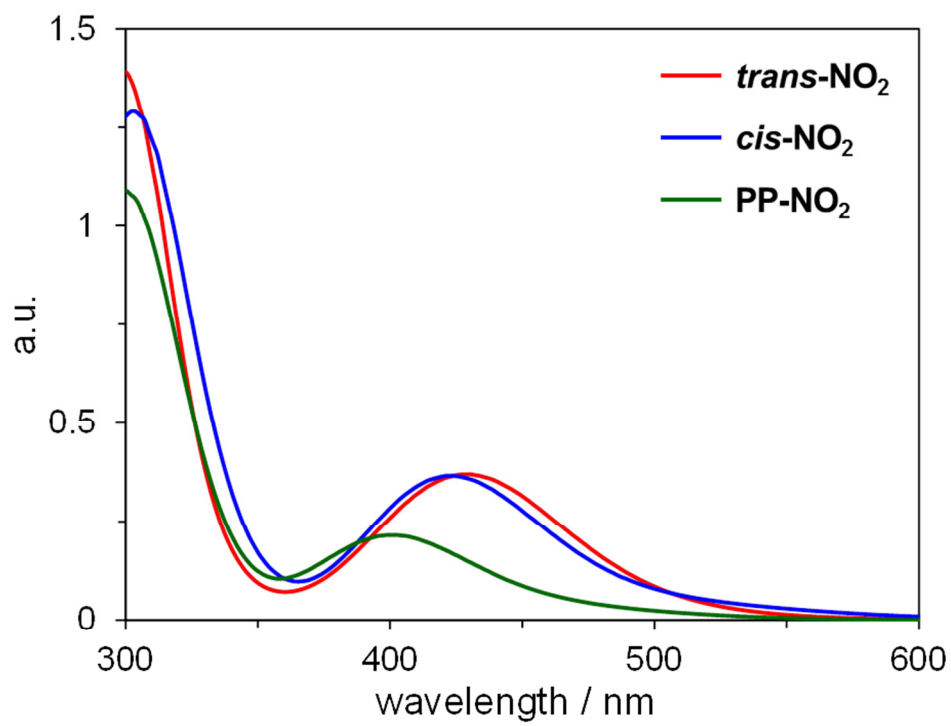
Figure S8 Simulated absorption spectra of *trans*-NO$_2$, *cis*-NO$_2$, and **PP-NO$_2$** in acetonitrile based on TD-DFT calculations.
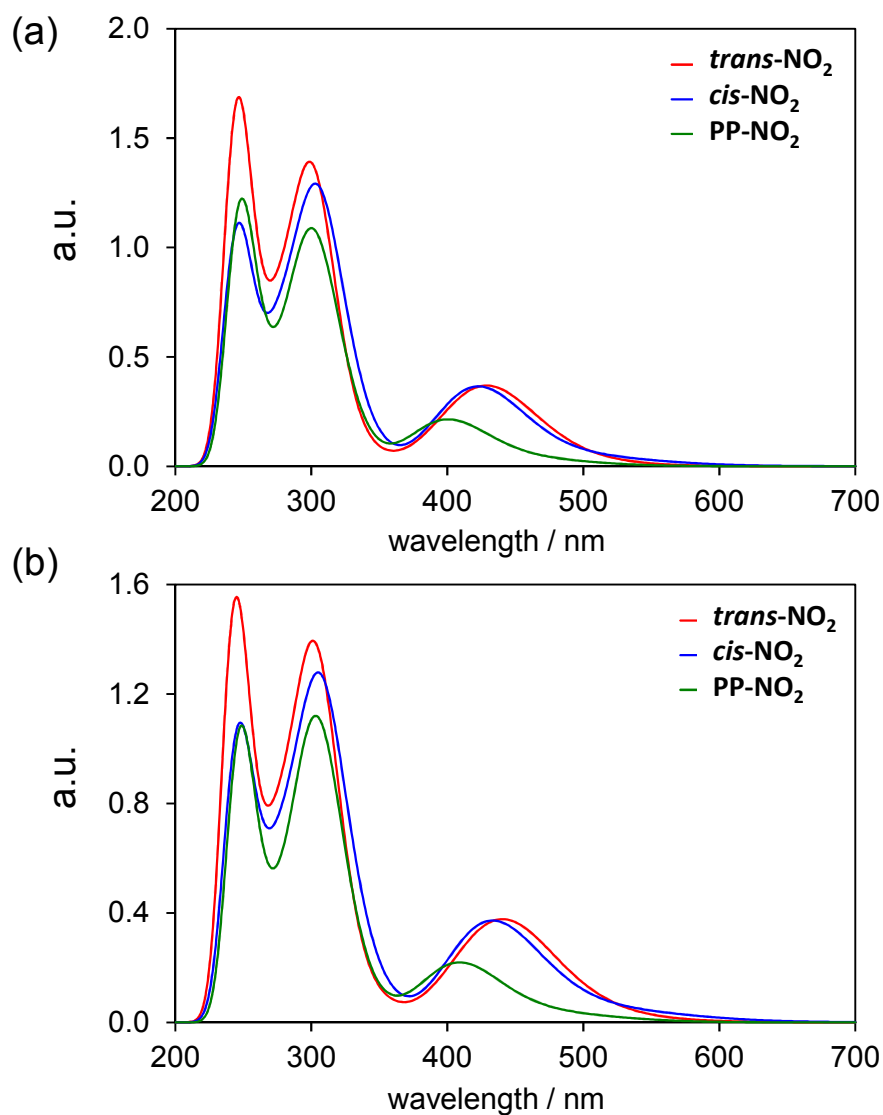
Figure S9 Simulated absorption spectra of *trans*-NO$_2$, *cis*-NO$_2$, and **PP-NO$_2$** in acetonitrile based on TD-DFT calculations at (a) B3LYP/LanL2DZ and (b) B3LYP/SDD level. The calculation using SDD and LanL2DZ afford the almost same results for all complexes.
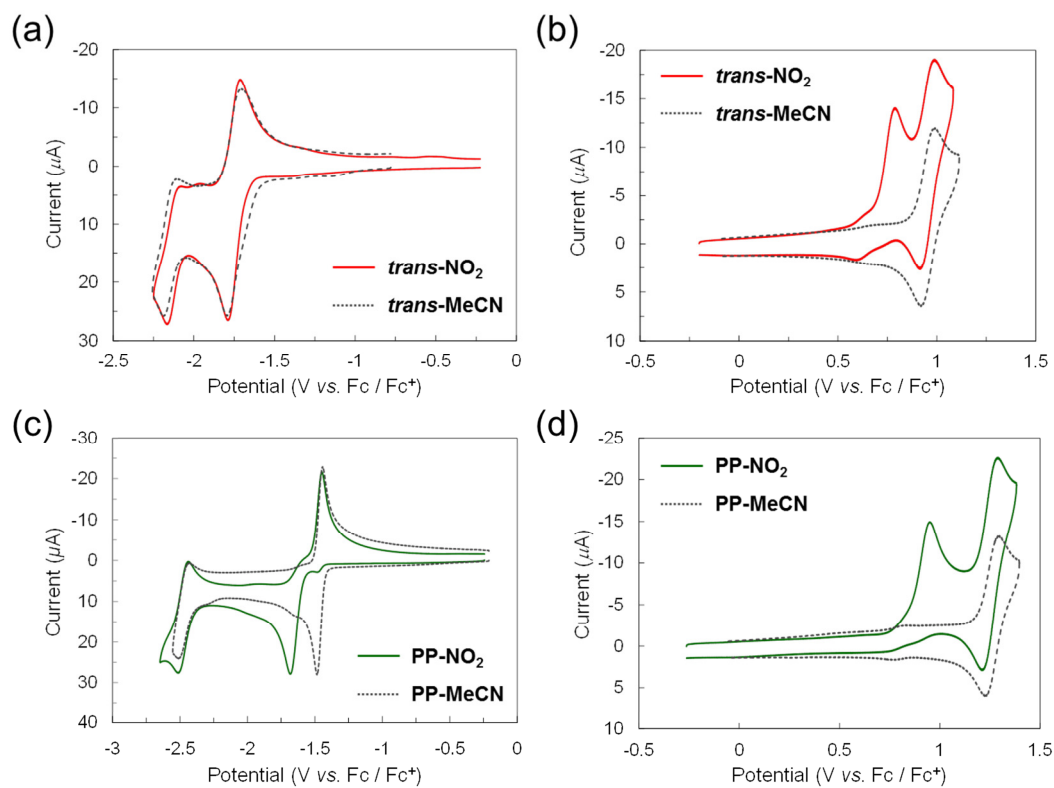
Cyclic Voltammograms

Figure S10 (a), (b) Cyclic voltammograms of *trans*-**NO₂** and *trans*-**MeCN** (0.5 mM) in 0.1 M TEAP/acetonitrile under an Ar atmosphere. (c), (d) Cyclic voltammograms of **PP-NO₂** and **PP-MeCN** (0.5 mM) in 0.1 M TEAP/acetonitrile under an Ar atmosphere (WE: GC, CE: Pt wire, RE: Ag/Ag⁺; Scan rate: 100 mV/s).
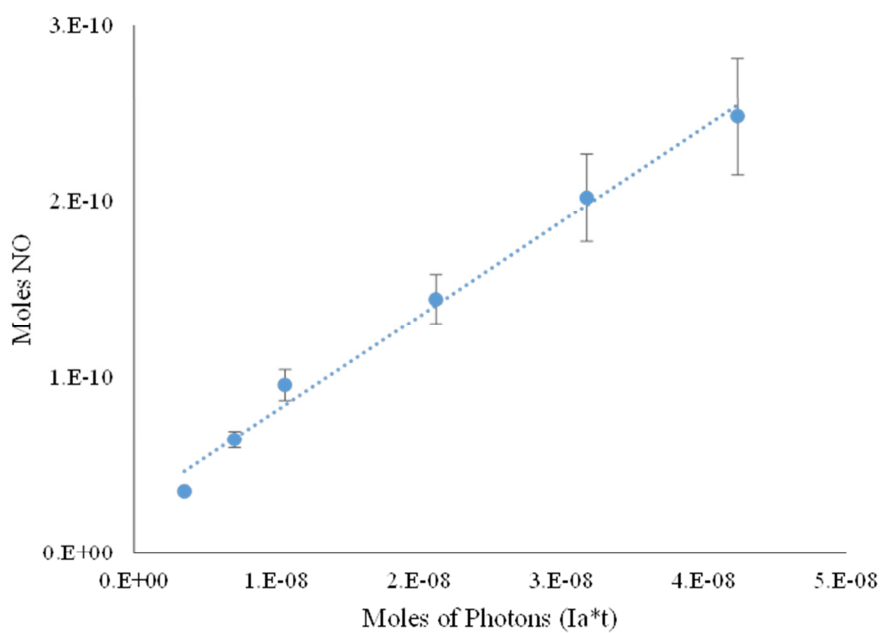
Photostability of *cis*-NO

Figure S11 Plots of moles of NO vs photons for the photorelease of ***cis*-NO** when irradiated at 365 nm under air conditions. Error bars reflect one standard deviation of the cumulative moles of NO produced over the duration of the experiment. The slope is equal to quantum yield. From these data, a quantum yield of 0.0048 under air conditions was calculated.
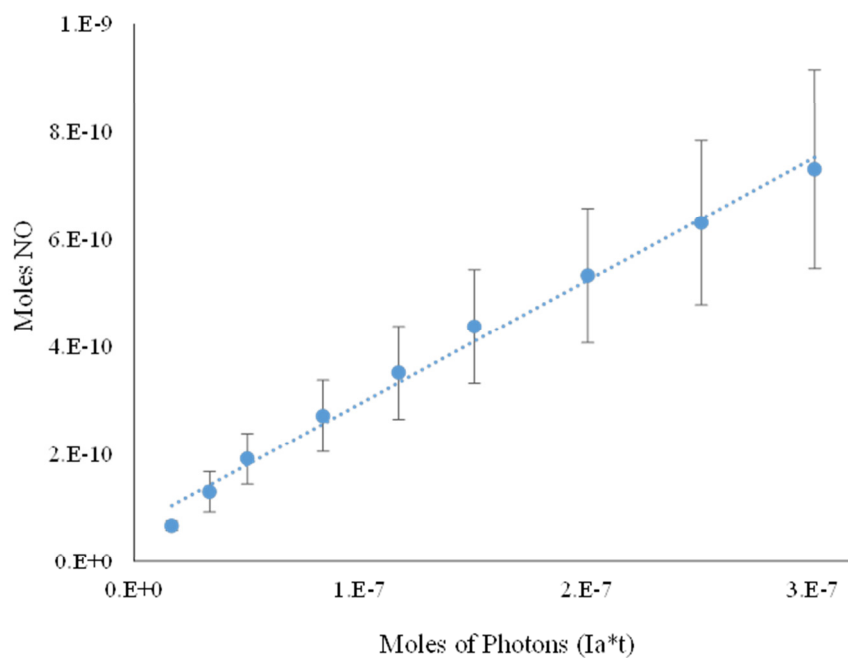
Figure S12 Plots of moles of NO vs photons for the photorelease of *cis*-**NO** when irradiated at 365 nm under helium. Error bars reflect one standard deviation of the cumulative moles of NO produced over the duration of the experiment. The slope is equal to quantum yield. From these data, a quantum yield of 0.0025 under helium was calculated.
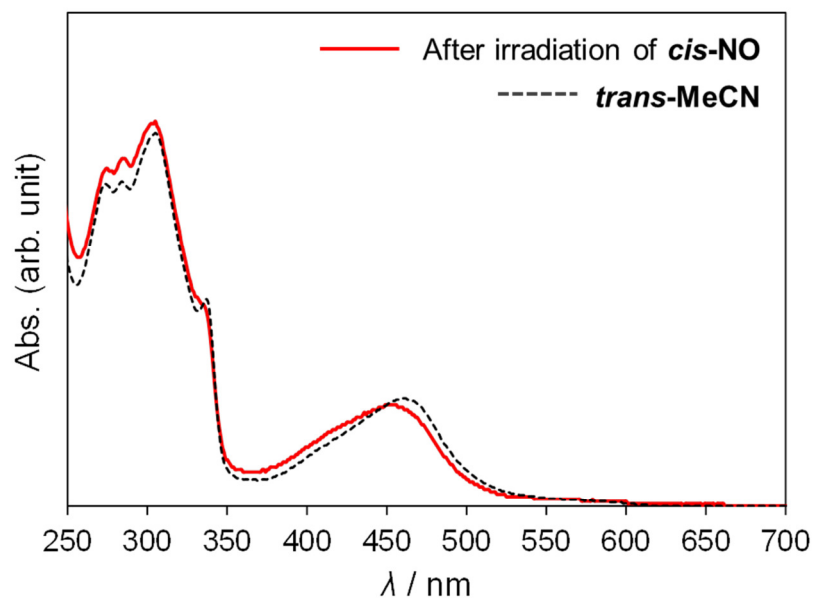
Figure S13. A UV-vis absorption spectrum of *cis*-**NO** in ethylene glycol after photoirradiation of 355 nm laser for 2048 times (pulse width = 5 ns, beam diameter incident on the sample = 6 mm, repetition rate = 5 Hz) and that of *trans*-**MeCN** in ethylene glycol at room temperature.
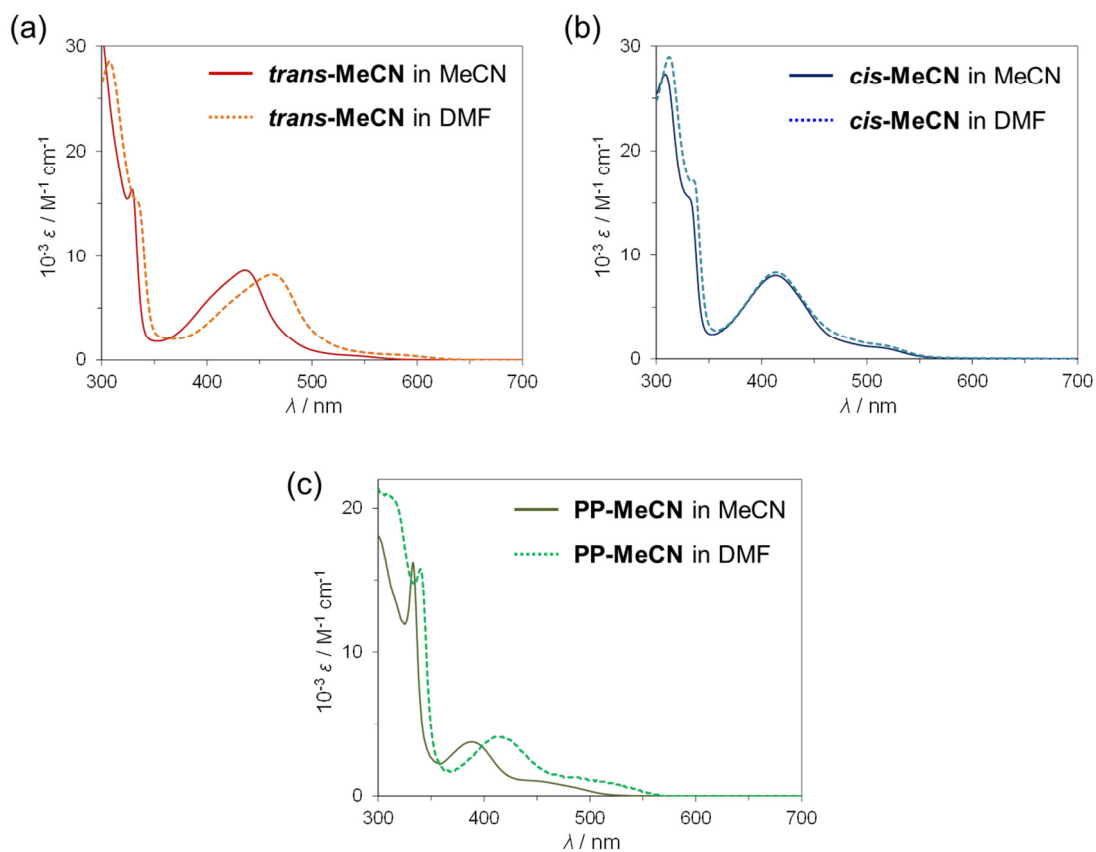
Stability of MeCN complexes

Figure S14 UV-vis absorption spectra of *trans*-**MeCN**, *cis*-**MeCN** and **PP-MeCN** in acetonitrile and DMF at room temperature. The UV-vis spectra indicate that the acetonitrile ligand of *trans*-**MeCN** and **PP-MeCN** can easily undergo a ligand substitution and form *trans(P,DMF)*-[Ru(trpy)(Pqn)(DMF)](PF$_6$)$_2$ (*trans*-**DMF**) and [Ru(trpy)(dppbz)(DMF)](PF$_6$)$_2$ (**PP-DMF**), whereas that of *cis*-**MeCN** is barely substituted.

Single Crystal X-ray Structure Determination

Table S2 Selected bond distances (Å) and angles (°) for *trans*-NO$_2$, *cis*-NO$_2$', and PP-NO$_2$

trans-NO$_2$·CH$_3$CN		*cis*-NO$_2$'·0.5CH$_3$CN				PP-NO$_2$·2CH$_3$OH	
Ru1–N1	2.085(4)	Ru1–N1	2.1066(18)	Ru2–N6	2.1353(19)	Ru1–N1	2.125(2)
Ru1–N2	1.971(4)	Ru1–N2	2.0153(18)	Ru2–N7	2.0248(19)	Ru1–N2	2.020(2)
Ru1–N3	2.081(4)	Ru1–N3	2.1066(18)	Ru2–N8	2.1012(19)	Ru1–N3	2.095(2)
Ru1–N4	2.143(4)	Ru1–N4	2.1080(18)	Ru2–N9	2.1241(18)	Ru1–N4	2.124(2)
Ru1–N5	2.146(4)	Ru1–N5	2.0362(18)	Ru2–N10	2.0290(18)	Ru1–P1	2.2958(7)
Ru1–P1	2.2952(13)	Ru1–P1	2.2981(6)	Ru2–P2	2.3005(6)	Ru1–P2	2.3270(7)
N5–O1	1.199(6)	N5–O1	1.251(3)	N10–O3	1.253(3)	N4–O1	1.252(3)
N5–O2	1.246(6)	N5–O2	1.251(3)	N10–O4	1.253(3)	N4–O2	1.229(3)
N1–Ru1–N2	79.00(17)	N1–Ru1–N2	78.31(7)	N6–Ru2–N7	77.74(8)	N1–Ru1–N2	77.59(9)
N2–Ru1–N3	79.43(17)	N2–Ru1–N3	78.35(8)	N7–Ru2–N8	78.25(7)	N2–Ru1–N3	78.46(9)
N4–Ru1–P1	82.00(12)	N4–Ru1–P1	82.65(5)	N9–Ru2–P2	82.51(5)	P1–Ru1–P2	84.10(3)
O1–N5–O2	122.4(5)	O1–N5–O2	117.75(19)	O3–N10–O4	118.00(18)	O1–N4–O2	118.5(2)